Low friction and wear resistant coatings

Carvalho, Nuno Jorge Marcolino

4

MECHANICAL PROPERTIES OF WC/C MULTILAYERS

4.1 INTRODUCTION

Contact-induced fracture in coated systems is complex and controlled by the coating material itself, the substrate upon which the coating is deposited, and the interface(s) which bond the system together. Understanding the fracture mechanisms is critical to foresee how the coated system will perform in service. Nevertheless, because the coatings are used in applications where low friction is required, through-thickness cracking may be relatively unimportant, provided that the relaxation of any residual stresses (and membrane stresses) in the system does not decrease the hardness below acceptable levels. Moreover, the coated system should not detach from the substrate, thereby creating unwanted hard wear debris.

Ultra low load indentation (nanoindentation) experiments have become increasingly widespread to gauge the mechanical properties of coated systems. The appeal of this technique is that very low loads and displacements are available, enabling characterisation on a sub-micrometer scale. These features permit mechanical property data to be obtained from thin films not only in the microstructural and residual stress state in which they exist as coatings while on a substrate, but also in a regime where their properties should dominate.[1,2] The confrontation of load-displacement data obtained from nanoindentation

with *post mortem* observation of the indentations, using either scanning electron microscopy (SEM) or scanning force microscopy (SFM), reveals important aspects of the contact-induced fracture of coated systems.[3,4] However, complementary information is needed of the extent of any delamination at the indentation sites. Techniques such as scanning electron acoustic microscopy (SEAM)[5] and Nomarski interference light microscopy[6] have been used to examine delamination, although the resolution is found to be too low. In this thesis, a method for cross-sectioning the samples through the contact sites was developed (see chapter 2). It permits a direct observation of the fracture mechanism and thus, overcoming the lack of information obtained with the previous methods. Additionally, the method permits cross-sectional transmission electron microscopy of the nanoindentations to be performed. Thus, a better view of the interplay between the mechanical properties, the microstructure, and the chemical composition of the system can be achieved.

As these coatings are developed for applications where low friction to common counterface materials is required, it is of primary importance to quantify their friction coefficient. This is so, even when the tribological properties are critically influenced by the operating environment. For example, the relative humidity and temperature influences the sliding interface tribo-chemistry and the formation of transfer layers.[7,8]

This chapter presents a detailed study determining the sequence of fracture events of WC/C multilayers onto stainless and tool steel substrates. The use of different coating-substrate configurations revealed important clues with respect to the mechanical behaviour of the coated system. A thorough assessment on elastic, plastic, and fracture properties was performed by nanoindentation and rolling contact fatigue experiments. Advanced electron microscopy techniques were used to retrieve complementary information of the delamination mechanisms.

4.2 COATED SYSTEMS AND EXPERIMENTAL METHODS

The dissimilar coating-substrate systems employed to investigate the mechanical properties are presented in table 4.1. Substrates with both plate and ring shape were used. The coated systems with a plate shape were subjected to nanoindentation tests, whereas the rings were utilised for friction coefficient measurement and rolling contact fatigue experiments.

Table 4.1 *List of coated systems investigated.*

Sample ID (shape)	Substrate material	Substrate hardness HV [GPa]	Substrate pre-treatment	Substrate roughness R_a [µm]	Coating roughness R_a [µm]
S1 (Ring)	Stainless steel (AISI 304)	1.6	Polished	0.05	0.05
S2 (Plate)	Stainless steel (AISI 304)	1.6	Polished	0.03	0.05
T1 (Plate)	Tool steel (AISI D2)	6.8	Polished	0.07	0.06
T2 (Ring)	Tool steel (AISI D2)	6.8	Polished	0.03	0.03
T3 (Ring)	Tool steel (AISI D2)	6.8	Ground	0.1	0.1
T4 (Ring)	Tool steel (Vanadis 30)	8.8	Polished	0.13	0.12
T5 (Ring)	Tool steel (Vanadis 30)	8.8	Polished	0.06	0.07

Nanoindentation experiments were carried out on samples S1, S2, and T1 using a home-made apparatus with a Berkovich diamond tip, as described in chapter 2. Indentation cycles were made under displacement control to peak loads ranging from 10 mN to 1 N. For each load, a series of at least ten indentations were performed and a mean value for hardness and effective modulus was taken. The standard deviation was used as a measure for the experimental uncertainty.

The coefficient of dry friction was investigated using a pin-on-disc tribometer. Coated system T4 was selected as the test ring, while a pin with a radius of 4.6 mm, manufactured from 42CrMo4 steel was used as counterface material. The measurement was conducted at a constant sliding velocity of 0.1 $m.s^{-1}$ in laboratory air (about 40% relative humidity) and at room temperature (~20 ºC). The applied load on the pin was 50 N. According to the *Hertz* theory[9] of normal contact of elastic bodies, it creates an initial mean contact pressure of 92 MPa. The friction coefficient was recorded over 20 hours, corresponding to a sliding distance of 7200 m.

Rolling contact fatigue tests were performed with a modified pin-on-ring tester (shown schematically in figure 2.8). This equipment permits to characterise the adhesion strength of coated systems and the mechanism of failure under conditions of dynamic loading. The normal load, F_N, was applied through a pneumatic pressure unit in a range from 0.4 to 1.2 kN. This load range corresponds to a maximum contact stress ranging between 3.1 and 4.1 for bare substrate, and between 3.4 and 4.9 GPa for WC/C coated systems. The related maximum equivalent stress lies in the regime of elastic-plastic deformation of the substrate.

In the case of systems with high speed steel substrate (Vanadis 30) only one normal load of 1050 N was applied, corresponding to a maximum contact stress of 4.5 GPa. This value was selected in such a way that the maximum equivalent stress is about 95% of the substrate compressive yield strength. The tests were automatically stopped when either a 1% of the coating area had been exfoliated, establishing the coating fatigue lifetime, or a maximum of 500 hours running time was reached, corresponding to 15 million contact cycles.

4.3 NANOINDENTATION RESPONSE

4.3.1 ANALYSIS OF LOAD-DISPLACEMENT CURVES

Considerable insight into the behaviour of coated systems can be gained from their load-displacement response, especially when a comparison is made with that of the substrate alone. Figure 4.1 shows the load-displacement responses of the two substrate materials for two independent indentations. The responses are typical of ductile materials. The loading curves are parabolic and the unloading segment displays little elastic recovery of the indentation depth. Plastic deformation is evident even at lower loads, being more pronounced on 304 stainless steel due to its higher ductility.

The load-displacement curves of the coated systems are shown in figure 4.2. The response, compared to the substrate material, demonstrates that the load-displacement curve for low peak loads exhibits an increased amount of elastic recovery on unloading, establishing that a higher proportion of the deformation is accommodated elastically. This is observed by smaller displacements at maximum load, and reductions in the elastic and plastic works of indentation.

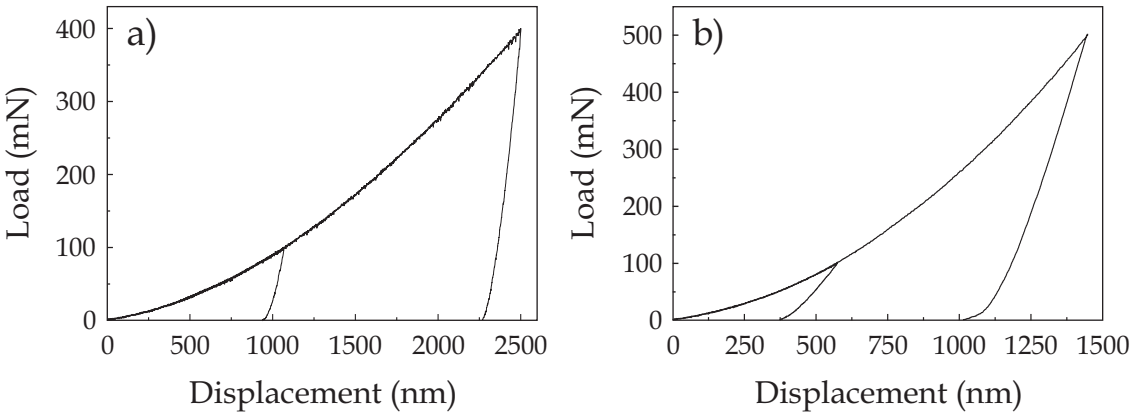

Figure 4.1 *Nanoindentation load-displacement curves of the steel substrates:* (a) *indentations with peak loads of 100 and 400 mN on stainless steel;* (b) *indentations with peak loads of 100 and 500 mN on tool steel. The responses are typical of plasticity-dominated materials, showing a parabolic loading curve and an unloading segment more or less vertical.*

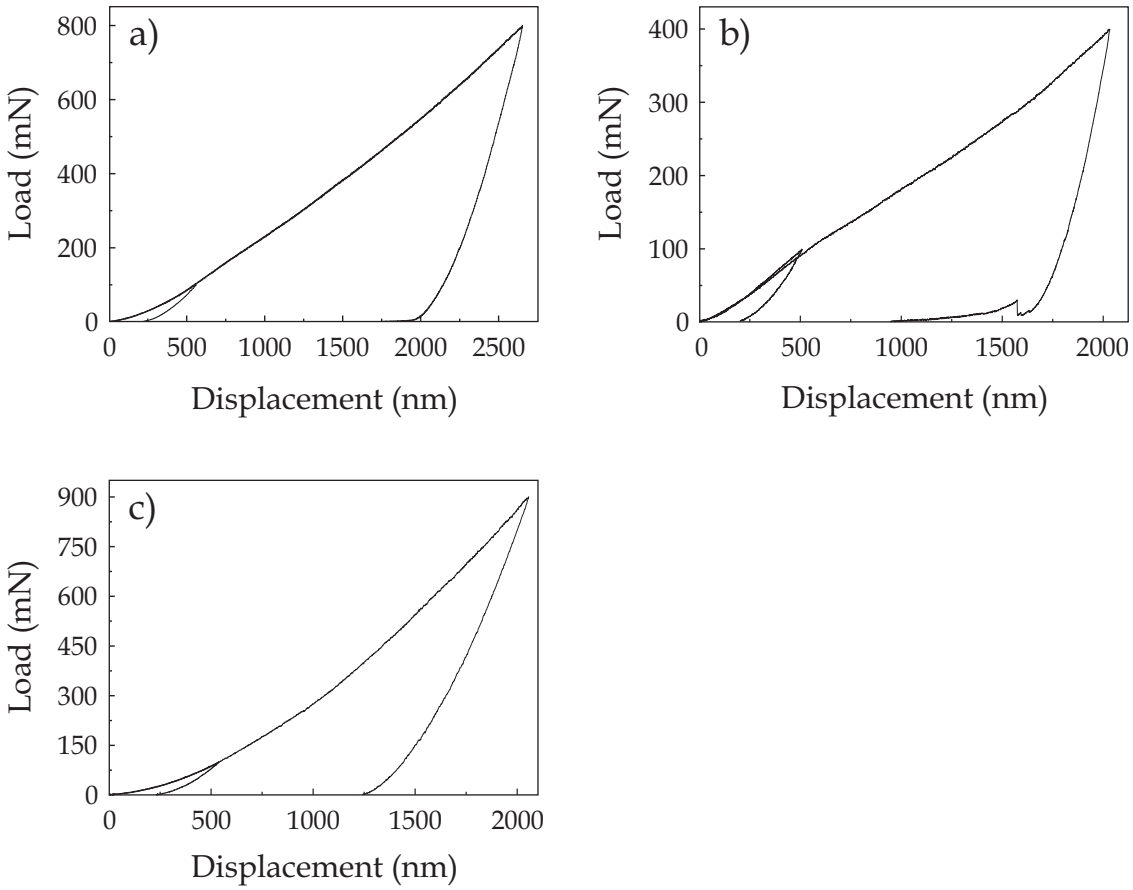

Figure 4.2 *Nanoindentation load-displacement curves of the three coated systems:* (a) *response of system S1 to peak loads higher and lower than the decrease in slope, which takes place at ~150 mN (best seen at a glancing angle);* (b) *response of system S2 for the same situation as described above, though in this case the change in slope occurs at ~120 mN. The last stages of unloading show the uplifting of the coating;* (c) *response of system T1 for indentations at two different peak loads showing no decrease in slope. Note the different values of peak loads that had to be used to achieve an equivalent maximum total surface deflection.*

Thus, the influence of the substrate is much reduced, evidencing that at these contact loads the response of the system is mainly characterised by the coating properties. On the other hand, at higher peak loads, however, corresponding to an indentation depth considerably lower than the coating thickness, the elastic recovery is more related to the substrate, indicating that the relative

contribution of the coating to the system has been reduced. The load-displacement curves displayed in figures 4.2a and 4.2b from WC/C onto stainless steel exhibits a discrete change in the slope of the loading curve at ~150 mN for system S1 and at ~120 mN for system S2. However, the WC/C onto tool steel does not exhibit such a change. SEM micrographs from system S1 and S2 showed that indentations whose peak load was lower than the value of decrease in slope exhibit no signs of coating failure, whereas for higher loads the indentation had always an annular crack around the periphery. The fact that the initial unloading contact stiffness from the load-displacement curve of figure 4.2b is not dominated by the modulus of the substrate (cf. figure 4.1a), indicates that the annular crack is not a complete through-thickness. Increasing the peak load, there is an additional flexing of the coating around the periphery of the impression and formation of more annular cracks. Then, the initial unloading contact stiffness approximates the one controlled by the modulus of the substrate. At ~700 mN the unloading is controlled only by the substrate modulus. In this situation it is believed that the first annular crack has developed completely through-thickness.

The nanoindentation response of coating system T1 did not show any change in slope for the load range employed in this study (10 mN up to 1N). Instead, the SEM micrographs from higher peak load indentations showed the presence of nested cracks following the indentation profile. Thus, the crack pattern is more related to the substrate deformation mechanism, rather than the one of the coating. Figure 4.3 presents SEM micrographs of nanoindentation response of the coated systems. The micrographs were taken from the indentation impression at the higher loads of figure 4.2. The existence of annular cracks in the case of stainless steel substrate suggests that the cracks have followed the locus of maximum tensile stress. This was generated around the outer periphery of the contact zone by the coating flexure and upthrust of the substrate material (pile-up) due to displacement by plastic flow.[6] Conversely, the nested cracks for tool steel substrate, indicates that the coating has been bent and stretched as the substrate yields and plastically deforms to accommodate the indenter displacements.[10] The characteristic behaviour of these systems can be attributed to good fracture toughness for radial fracture, despite the ready availability of nucleation sites for crack propagation. As a result, annular

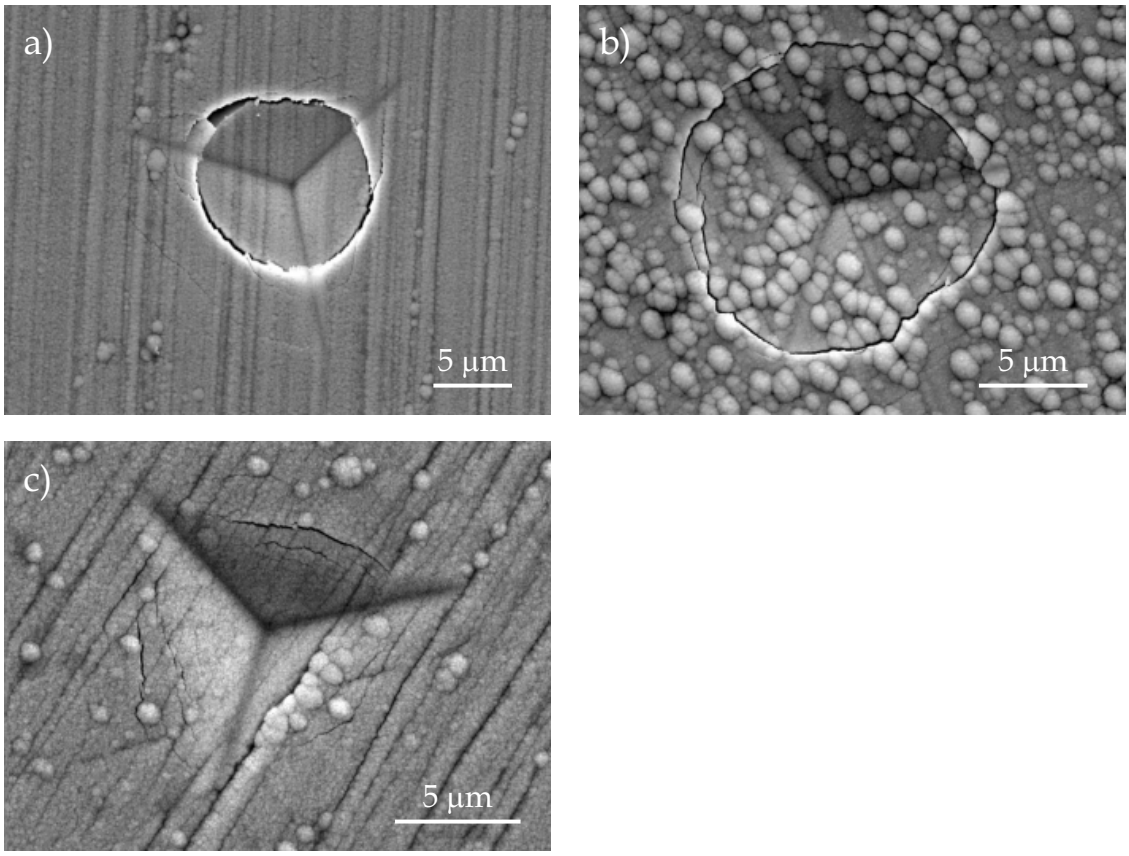

Figure 4.3 *SEM micrographs showing the indentation impression on coated systems.* (a) *800 mN nanoindentation on system S1;* (b) *400 mN nanoindentation on system S2;* (c) *900 mN nanoindentation on system T1. The first two display annular cracks, whereas the latter fractures through nested cracks.*

through thickness cracks occur before the necessary high critical stress for radial fracture has been reached.

The lower part of the unloading curve in figure 4.2b is of considerable interest. Since the nanoindenter utilised in this study is displacement controlled, any change in load applied to the tip is registered. Therefore, the load-displacement response gives indication that during the last stages of unloading the sample was relaxing elastically, and suddenly it tried to push the indenter out (increasing the load at the apex), as if the coating has had popped-up by propagation of a interfacial crack. To confirm this popping-up of the coating, confocal microscopy on the indentations was performed. Figure 4.4 shows a

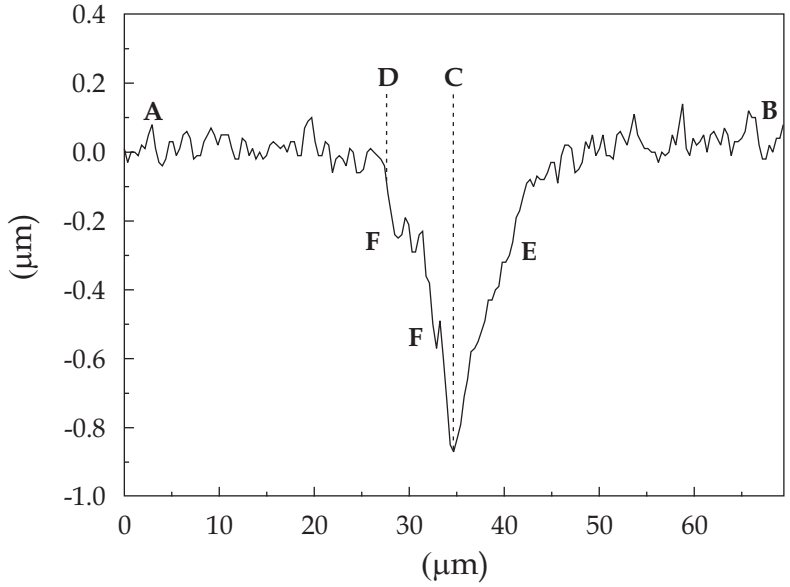

Figure 4.4 *2D-profile through one of the vertices of the indentation shown in figure 4.3b. From the profile it is possible to conclude that the area within the indentation contains more topographic information than evident from the SEM micrograph. The change in slope at the annular crack (D) is clear. Also, the radius (DC=6.9 μm) agrees well with measurements from the SEM micrograph. The residual indentation depth (~870 nm) is lower than the value obtained from the P-δ graph of figure 4.2b (~ 1000 nm). [Key: C=indentation centre; D=annular crack; E=radial plastic groove running along the indentation diagonal; F=upthrust edge of plastic impression within the indentation area; A,B=undisturbed sample surface].*

cross-section from the indentation shown in figure 4.3b and drawn to pass through one of the vertices. The right and left hand edges of the profile (*A* and *B*) are the flat region of coating well away from the indentation itself. There are two vertical lines on the profile; one (*C*) which passes through the bottom of the indentation centre while the other (*D*) is drawn at the position of the annular crack. The distance measured horizontally between these two lines correlates well with the same measurement taken from the SEM micrograph. Thus, despite the deceptively flat appearance of the SEM image, the profile clearly shows that the central region within the annular crack is depressed to various depths compared to the mean level of the coating. However, it is markedly shallower than the residual indentation depth of ~1 μm, indicating that after the

indenter is removed, the coating surface within the annular crack is displaced above the residual position. This clearly establishes that the disc-like portion of the coating within the annular crack must be decoupled from the substrate. The fact that debonding of this section of coating from the substrate has not been accompanied by the disk either falling out or popping up above the original surface, suggests that is still mechanically interlocked in some way either to the substrate or to the rest of the coating.

Popping-up of the coating did not occur beyond a certain maximum applied load (~500 mN), presumably due to an almost complete through-thickness annular crack. Coated systems S1 and S2 share the same substrate and both have a chromium interlayer. Therefore, the evidence that uplifting of the coating had only occurred for coated system S2 suggests that the failure mechanism was decohesion within the coating, rather than debonding from the substrate. Moreover, *Whitehead et al*.[10] have proposed that interfacial crack propagation is more likely to take place in systems with a brittle substrate, where fracture is driven by the stored elastic energy across the interface. To certify that decohesion took place only for coating system S2, the other systems were subjected to the maximum load available from the nanoindenter. As it can be clearly observed from Figures 4.2a and 4.2c, the nanoindentation responses do not present evidence of coating delamination upon unloading.

Hainsworth et al.[11] have proposed that changes in the slope of load-displacement squared *(P-δ^2)* can be used to assess the transition between the different regimes of coated system behaviour. In this model, the load-displacement squared curve shows three distinct regions. Initially, the indenter should just probe the properties of the coating, which should be reflected by a straight line. Then, there is a transition region where the properties of the coating and substrate are probed. Subsequently, the curve should again be a straight line reflecting the properties of the substrate alone. Figure 4.5 shows the *P*-δ^2 data for indentations on the coated systems (obtained from the *P*-δ curves of figure 4.2). The *P*-δ^2 graphs of figures 4.5a and 4.5b displays the three distinct regimes of coated materials. The first regime is characterised by a straight line segment (from the origin to *A*), which is believed to be related to the coating properties. It should be noted that *A* is lower than the load at which fracture occurred (*C*). Thus, while *C* is obvious in the *P*-δ curve, it is simply a characteristic of the

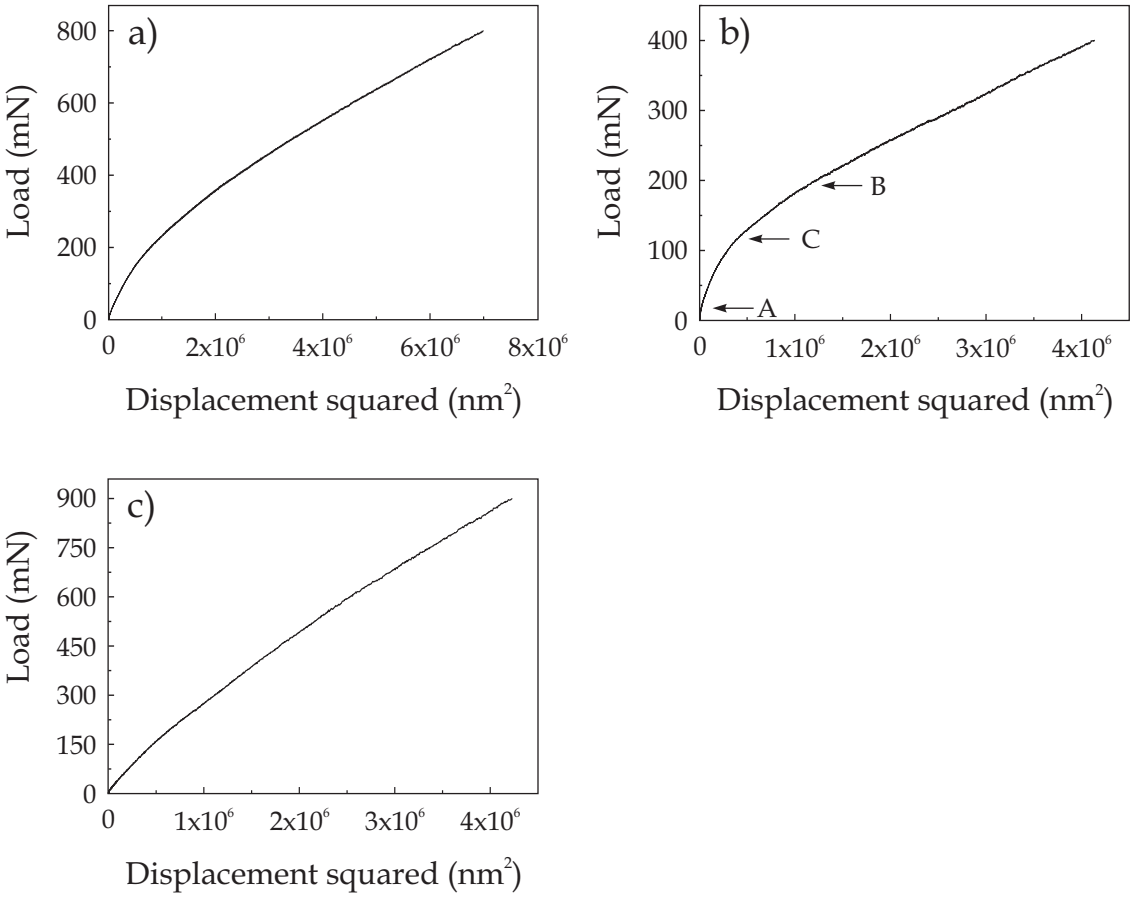

Figure 4.5 *Load-displacement data corresponding to the higher peak loads of figure 4.2 replotted as load-displacement squared. Curves* (a) *and* (b) *are of systems S1 and S2, respectively. As these systems have a stainless steel substrate, the transition between the differing regimes of behaviour is undoubtedly observed. Curve* (c) *of system T1 does not displays as clearly the change of coating-substrate domination.*

annular crack occurring and it is not necessarily the end of the regime in which the P-δ curve is dominated by the coating. However, on the P-δ^2 curve, it is *A* that is obvious and *C* that only occurs as a small discontinuity. Thus, the P-δ^2 graph is a more sensitive tool for exploring the coating regime. The transition region between the coating only dominated and substrate dominated is labelled *A-B*. It is where the properties of both the coating and substrate are relevant. Within this region, the substrate had deformed plastically causing the coating to crack around the indentation periphery,

originating the annular crack. At large displacements, after *B*, the fractured coating will play an insignificant role in supporting the applied load. Therefore, a second straight line segment emerges, whose slope is approximately controlled by the substrate properties, representing the last regime. The small non-linear segment at the beginning of the graph is thought to be caused by a combination of tip shape imperfections and any elastic-only deformation of the coating as the tip first makes contact with the surface.[12] The P-δ^2 graph displayed in figure 4.5c, for coated system T1, does not clearly reveal the transition between the coating and substrate domination of the indentation response. Therefore, when the coating fracture is via nested cracks instead of annular cracks, the membrane stresses in the coating that supports a fraction of the load still plays a role in the system response, even at peak loads as high as 0.9 N.

4.3.2 MECHANISMS OF CRACK PROPAGATION

Cross-sectioning the nanoindentations was aimed at confirming that the failure mechanism was indeed decohesion within the coating. Figure 4.6 shows a SEM micrograph of a cross-sectioned 400 mN nanoindentation. The area where the micrograph was taken can be precisely determined from the diameter of the annular crack and the orientation of the indenter tip. The presence of a brighter band in the coating is due to a higher tungsten concentration (for more details see chapter 3). The micrograph clearly establishes that the uplifting of the coating occurred not by interfacial fracture, but by crack propagation inside the coating. Further, the cracks produced by tensile stresses, namely, the one related to the indentation apex and the through-thickness are also observed. It is noteworthy that the elastic strain energy stored within the coating due to bending is not enough for, upon unloading, debond the chromium interlayer from the steel substrate. Instead, as shown in figure 4.7, the energy was released by crack propagation in the carbon lamellae of the WC/C multilayers, where crack arrest occurred when the system reached equilibrium (see figure 4.7a). The crack propagated normal to the multilayers through carbon-enriched defects present in the coating, as seen in figure 4.7b. These defects were created either by substrate surface irregularities or simply by the top morphology of the

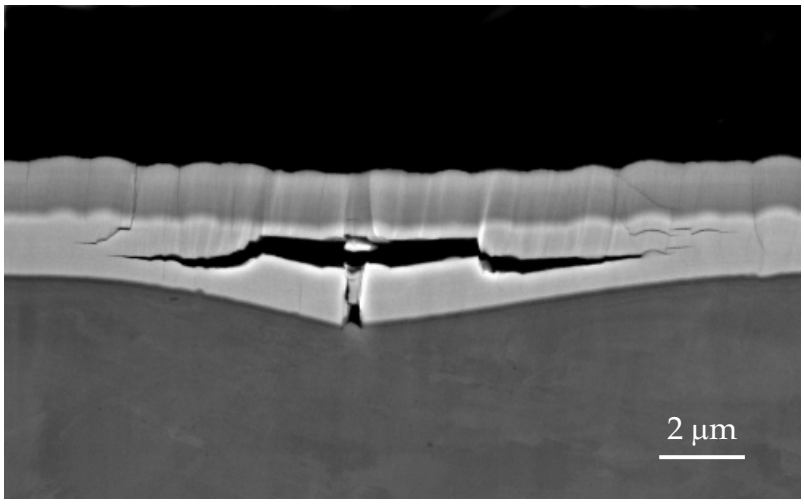

Figure 4.6 *SEM micrograph displaying a cross-section of a 400 mN nanoindentation on system S2. The coating contrast is related to dissimilarity in tungsten concentration, where brighter corresponds to a higher concentration. The right and left hand side cracks normal to the surface are from the annular crack formed around the indentation periphery, while the central crack was created by the indenter apex. The micrograph clearly establishes that the crack propagation occurred inside the coating.*

chromium columns (see chapter 3). The explanation for crack propagation in the carbon lamellae (and ultimately leading to decohesion) of coated system S2, and not also of system S1, is related to their multilayer microstructure. As is explained in chapter 3, system S2 has a sharper interface between the lamellae (in contrast to the rather diffuse one of system S1). This difference in atomic mixing at the interface (cf. figure 3.7) is thought to be important for crack propagation. Moreover, the existence of an intermediate WC layer in the coating system S1 proves to be effective in supporting a fraction of the load and promoting the adhesion between the multilayers and the remaining coating.

4.3.3 SEQUENCE OF DEFORMATION EVENTS

The sequence of deformation events occurring during indentation is illustrated schematically in figure 4.8. Initially, only the coating deforms elastic-plastically (as is confirmed by the initial linear portion of the P-δ^2 curve). Hence, the

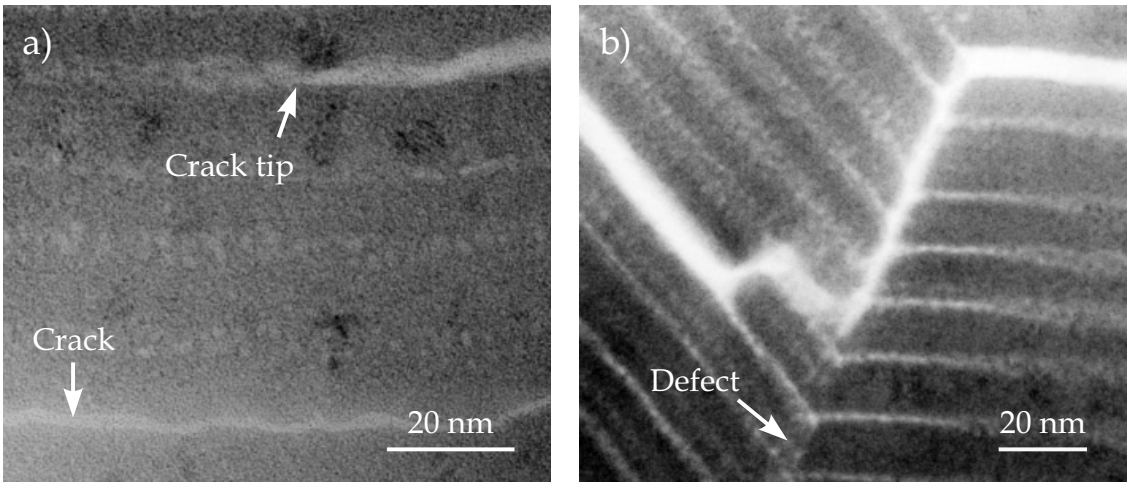

Figure 4.7 *Cross-sectional TEM images of the crack path. The images unequivocally confirm that crack propagates in the carbon lamellae of the multilayer and glides through carbon-enriched defects.*

coating is deforming in response to the maximum Hertz-like shear stress that lies well within the coating depth. As the shear stress will decrease with depth,[9] it is apparent that the maximum value experienced by the substrate at this load is not high enough to yield.

Beyond *A* on the P-δ^2 curve, the substrate commences to experience a sufficiently high shear stress for plastic yielding. This requires the coating to flex and bend to conform to the subsurface deformation. However, the shear stresses in the coating are only large enough to cause plastic flow in an area immediately around the axis of the contact and along the indenter edges. At the same time, as the coating is forced to bent to follow the substrate deformation and pile-up, significant tensile stresses around the outer periphery of the contact zone in an approximately circular pattern are being generated. This corresponds to the region *A*-*C* on the P-δ^2 curve.

At a known, but slightly variable load, (point *C*), the tensile stress reaches a maximum value, causing the coating to crack around the indentation periphery, resulting in an annular crack. Presumably at this critical load, the tensile stresses beneath the indenter apex are sufficiently high to onset the crack

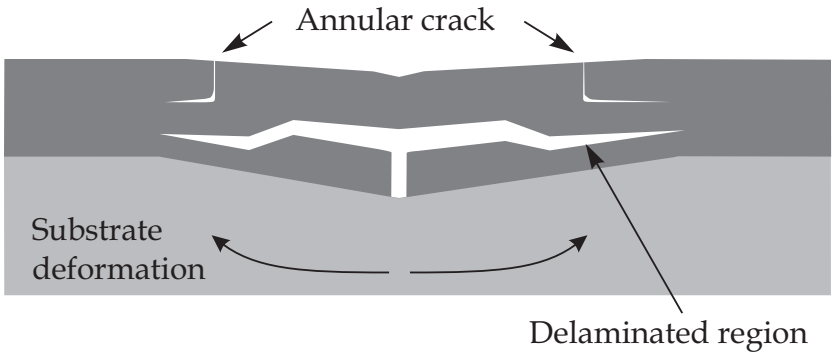

Figure 4.8 *Schematic diagram of the indentation-induced cracks which form on coated system S2.*

propagation normal to the coating-substrate interface (this assumption was confirmed experimentally by cross-sectioning a 200 mN nanoindentation). Increasing the load, the coating still play some role in the deformation mechanism until the third regime in the P-δ^2 curve is reached. Beyond that, (point *B*), the coating confined by the annular crack retains only a small portion of the membrane stresses and the substrate dominates the system response to deformation. Increased loading causes further annular cracks to occur as a larger proportion of the coating is bent into the substrate.

When the load is released, the slope of the initially unloading curve is constant due to the elastic recovery within the indentation. However, during the last stages of unloading very significant levels of elastic recovery occur followed by a sudden increase of the load at the indenter apex, corresponding to crack propagation inside the carbon lamellae parallel to the interface. The crack propagation is driven by the elastic strain energy stored within the coating free from the annular crack, i.e. the portion of the layer thickness beneath the through-thickness annular crack tip. The annular crack tip is always deflected outwards from the indentation impression. The cracks propagate until the system reaches equilibrium, which occurs further than the position of the annular crack. The non-observance of coating uplifting for peak loads above ~500 mN, is thought to be related to the elastic strain energy stored by bending of the small coating fraction beneath the annular crack tip. This energy is not

enough to overcome the carbon cohesive energy and the energy necessary to push the coating volume (bounded by the annular crack) upwards.

4.3.4 HARDNESS AND MODULUS

Taking into account the considerations drawn in chapter 2 on the influence of pile-up in quantifying the hardness and elastic modulus, all the indentations performed on the coated systems and substrates were checked for material pile-up. It was found that only the stainless steel substrate presented a large amount of pile-up around the hardness impression. Consequently, the hardness values measured for the coated systems might be considered being accurate. Compositional hardness values measured as a function of peak load for as-deposited WC/C onto steel substrates are shown in figure 4.9. In the range of low loads, the hardness values of the coated systems are similar. It validates the idea that the properties of the coatings can be measured at these depths of indentation. Thus, the hardness of WC/C can be estimated to be about 14 GPa, a value within the 10 to 40 GPa commonly reported for hard hydrogenated amorphous diamond-like coatings.[13-15] It is also interesting to analyse the hardness behaviour with peak load. For coated system T1 the hardness is approximately constant. Therefore, the presence of nested cracks did not decrease the efficiency of the coating in supporting the load. Conversely, for systems S1 and S2 the appearance of annular cracks immediately decreased the ability of the coatings to support the load, and the properties of the stainless steel substrates start to come into sight. Further, the difference in hardness for systems S1 and S2 is associated with the structure of the coating itself, where for system S1 the presence of a WC interlayer promotes the load bearing capacity of the coating.

The effective Young's modulus values obtained as a function of peak load for the coated systems is shown in figure 4.10. Considering once more that the coating properties are probed at low loads, an effective modulus value of about 220 GPa can be obtained for the WC/C. For coated system T1, the modulus increased with the applied load approximating the values of the tool steel substrate, while for system S1 the value was almost constant. At low peak loads, system S2 had a higher effective modulus. This is thought to be due to

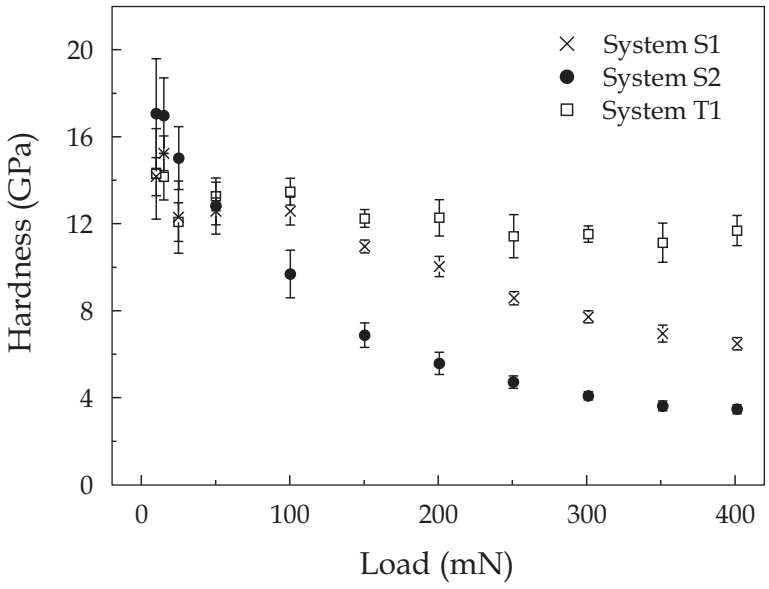

Figure 4.9 *Mean compositional hardness values of the coated systems obtained from nanoindentation as a function of peak load.*

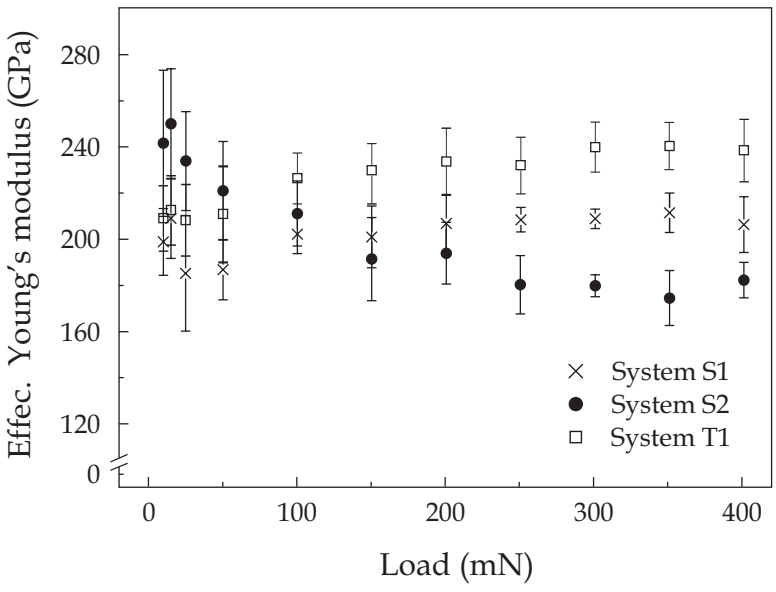

Figure 4.10 *Mean effective Young's modulus values of the coated systems obtained from nanoindentation as a function of peak load.*

dissimilarities in the WC/C multilayers, where the thicker WC lamellae could have increased the stiffness. To some extent, the scatter observed in the hardness and modulus values obtained at low peak loads is related to the place where the indentation is performed.

When a nanoindentation is performed on a defect-free region the coating can deform under load to accommodate the indenter without failure due to the bending stresses generated. This is achieved by the shear that occurs in the elastic lamellae (carbon) allowing the brittle ones (WC) to slide over each other in the manner of a multileaf book when bent.[16] When nanoindenting on a surface groove, such as the one in figure 4.11, the defect in the coating inhibits sliding of the lamellae causing a localised increase in hardness. Logically, this effect is not observed at higher loads, consequently a smaller deviation in the hardness and modulus values is obtained.

4.4 TRIBOLOGICAL PROPERTIES

4.4.1 FRICTION BEHAVIOUR

The sliding wear test showed that the WC/C multilayers have a low friction coefficient against steel. The variation of friction coefficient as a function of sliding distance is displayed in figure 4.12. A running-in period of about 2000 m with a higher coefficient of friction is identified. This high value gradually decreases with increasing sliding distance, achieving a relatively steady state. However, it seems that the value would further decrease with sliding distance until the multilayer would completely wear out.

For most sliding contact interfaces the extent of friction is controlled by a combination of physical, chemical and mechanical interactions at the microcontact interface.[17] Physically, the surface roughness is of major importance, since a rougher surface results in higher ploughing, and hence higher friction. Chemically, the amount of interactions between the rubbing surfaces may govern the extent of adhesive bonding across the interface. The mechanical interactions of the lamellar coating also influence the friction. When interposed between two sliding surfaces, the lamellae shear with relative ease,

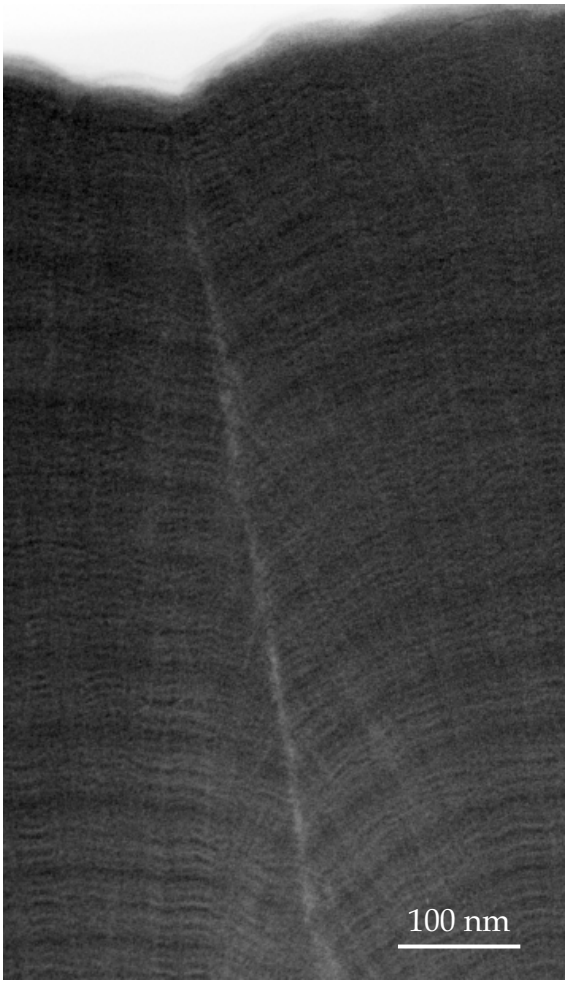

Figure 4.11 *Cross-sectional TEM image of the WC/C multilayers from the coated system S1 showing a surface groove created by a through-thickness defect.*

hence providing low friction. Therefore, to understand in more detail the mechanisms controlling friction, the sliding contact interfaces were analysed. As is disclosed in figure 4.13, the worn coating exhibits a very smooth surface topography without the formation of tribo-film. The only exceptions are the deeper surface grooves, where the coating is virtually intact, resembling the as-deposited topography (cf. figure 3.2). Even though not directly observed by the present test results, it is believed that the coating wear takes place in two steps; during the running-in period the surface asperities caused by the deposition technology are polished away leading to the initial increase in friction

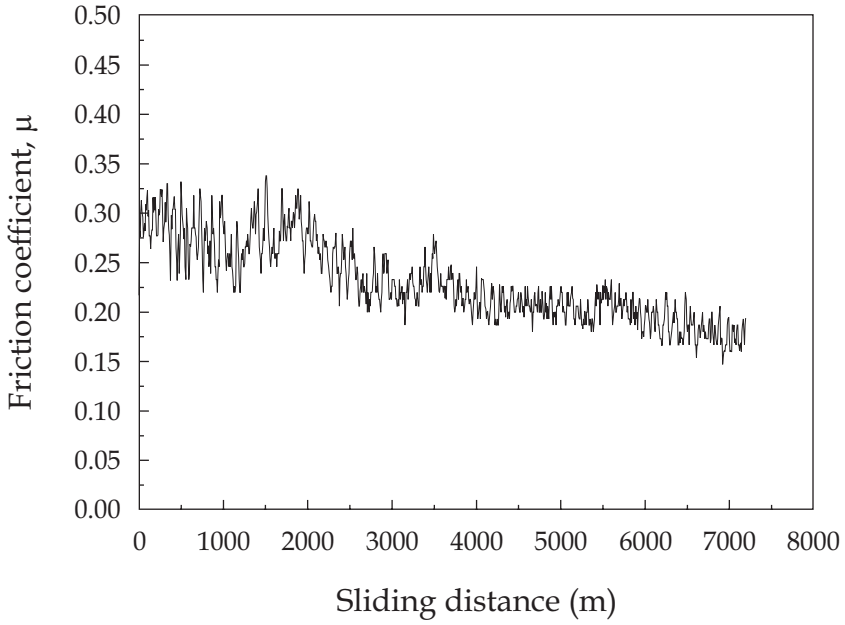

Figure 4.12 *Variation of friction coefficient of WC/C multilayers during sliding against a steel pin.*

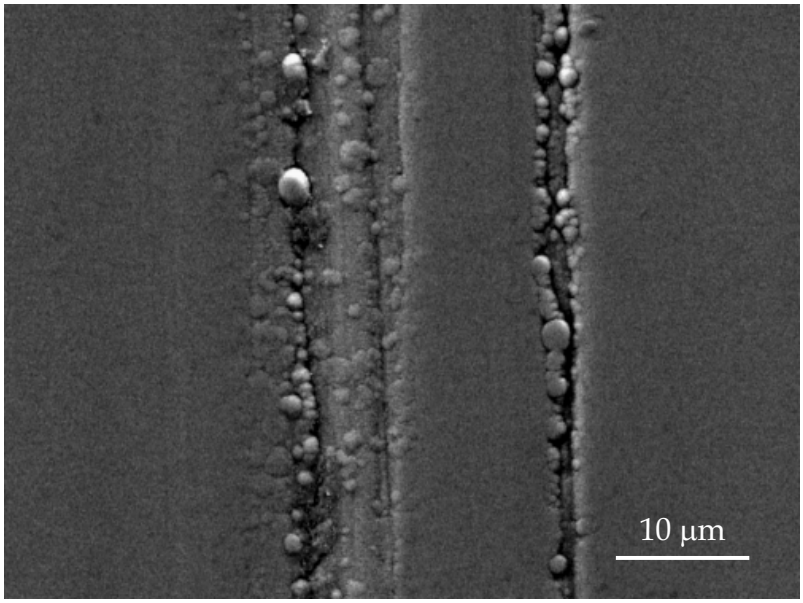

Figure 4.13 *Characteristic worn surface of the coated ring after sliding against a steel pin. The polishing wear mechanism led to a smooth surface, though the as-deposited morphology still can be seen on the unworn grooves.*

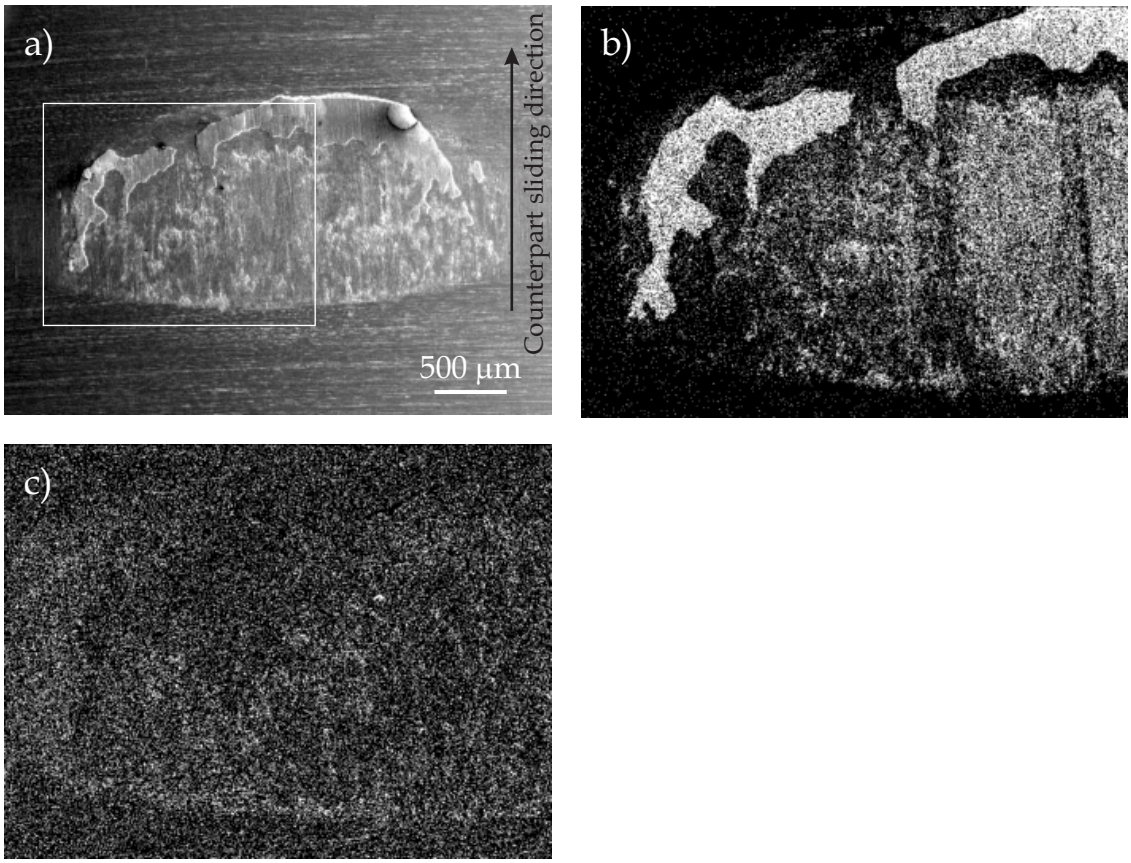

Figure 4.14 (a) *SEM micrograph of the wear scar with transfer layer formed on the steel pin after sliding against the coated ring.* (b) *EDS W-map of the transfer layer from the area depicted in the SEM micrograph.* (c) *C-map of the same area.*

coefficient. Then, the wear of the surface at the steady state occurs by smearing out of material from the coating, and transfer to the steel pin contact surface. As long as this slippery transfer layer is maintained, a low friction coefficient and long wear life is attained. The driving force for this smooth material transfer, instead of third body formation (wear debris) and sheared surface, seems to be the lubricating effect of the carbon lamellae. Thus, the adhesive and cohesive properties of the coating control the wear rate.

Microscopic observation of the steel pin after testing showed a wear scar with material transfer layer, see figure 4.14a. The transfer layer is spread all over the wear scar. However, there is also a long streak of material with an orientation

normal and facing the sliding direction, covering the entire width of the wear scar. The streak has a gradient in thickness, increasing from the inner to the outer side. This indicates that material is being trapped there during the sliding motion. Figures 4.14b, and 4.14c are EDS maps of tungsten using the M peak of 1.775 keV and carbon using the K peak of 0.282 keV, respectively. The maps were performed on the selected area from the SEM micrograph, and suggest that the streak has a tungsten character. According to the carbon map, this element is present all over the pin, even though it is possible to see very faintly the morphology of the wear scar, giving indication of a localised higher concentration of this element. Therefore, both tungsten and carbon are transferred from the multilayers to the pin, providing a self-lubricating mechanism and consequently a low friction coefficient.

4.4.2 ROLLING CONTACT FATIGUE

Rolling contact fatigue (RCF) tests were performed on coated systems T2, T3, T4 and T5. As listed in table 4.1, the differences among the rings include the substrate material, pre-treatment, and average roughness, rather than the coatings microstructure. They all have a microstructure similar to the one of system S2 (see chapter 3 for more details).

Upon testing the influence of the pre-treatment of the substrate and contact stresses, it was found that none of these parameters affected substantially the fatigue lifetime of the WC/C coated systems. On the other hand, when tests were performed at a single contact load on systems with identical polishing pre-treatment, but with a different substrate roughness, the fatigue lifetime was influenced noticeably. As seen in figure 4.15, the fatigue lifetime decreases with increasing substrate roughness.

It was possible to assess the fatigue damage mechanism by monitoring the RCF test through visible inspection combined with a registration of the vibration level. Figure 4.16 shows the percentage of the coating total area damaged *versus* the lifetime for two coated systems. The onset of fatigue is immediately after the start of the test by removal of small chips and grows steady at a slow rate, as the chips develop towards large damaged areas. This is in contrast with the

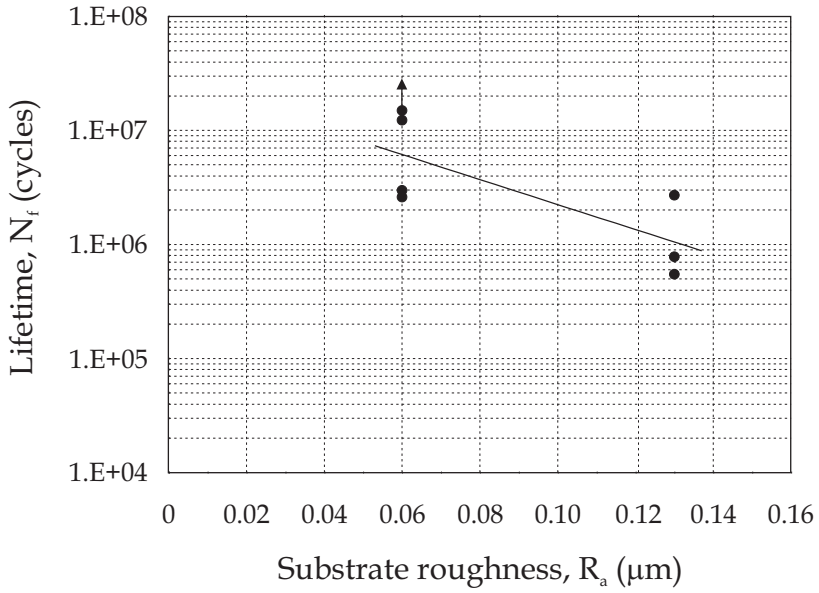

Figure 4.15 *Rolling contact fatigue results of WC/C onto polished steel substrates. All tests were subjected to a normal force, F_N, of 1050 N. The arrow indicates a test that was automatically stopped after 500 hours running time without fatigue failure.*

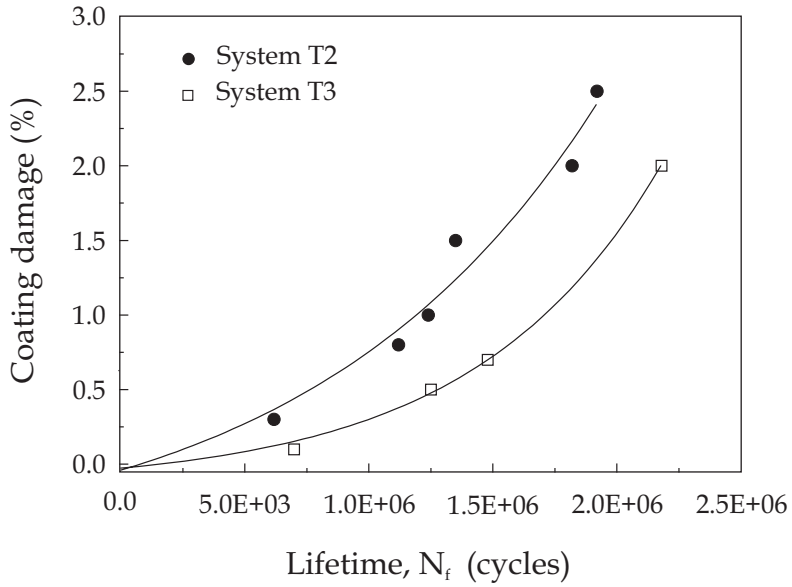

Figure 4.16 *Growth of fatigue damage in systems T2 and T3. The onset is immediately after starting of the test and grows slowly. The normal load applied on both systems was 1200 N.*

behaviour of other coatings, where chipping develops very fast into large spalling areas (see chapter 6).

The cross-sectional SEM micrograph of figure 4.17 gives an indication of the mechanism of chipping removal. It is suggested that the failure is due to surface crack initiation and propagation. During rolling contact, cracks propagate into the coating producing a localised exfoliation. A point of interest is the evidence of crack deflection at the chromium layer, indicating that the failure is due to the cohesion of the coating, rather than due to the adhesion along the interface. The decohesion nature of the fatigue is most probably due to tensile stresses arising in the coating because the compressive stresses of the WC/C multilayers are very low, being in the range of 0.9 to 1.5 GPa.[18] Altogether, the above observations confirm a parallelism between the rolling contact fatigue experiments and nanoindentation testing (cf. §4.3.2).

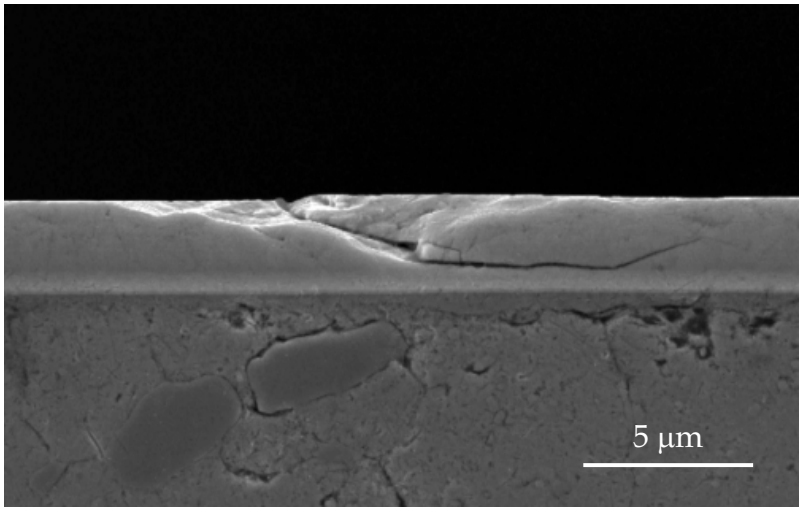

Figure 4.17 *Cross-sectional SEM micrograph of system T2 displaying cohesive failure of the coating due to rolling contact fatigue.*

4.5 CONCLUSIONS

In this chapter the nanoindentation response, friction coefficient and resistance to rolling contact fatigue of WC/C multilayers, deposited onto stainless steel and tool steel substrates have been investigated. The results are analysed and discussed with the support of planar and cross-sectional electron microscopy observations. The main conclusions are:

- Whenever the load-displacement curve shows a discrete change in slope, annular cracks around the indentation periphery are present;
- The deformation mechanism of coated systems depends on the substrate plastic properties. For stainless steel substrates, annular cracks are formed, while for tool steel, nested cracks are created;
- Combined analysis of P-δ and P-δ^2 curves enables a more comprehensive characterisation of the systems behaviour;
- The nanoindentation response gives accurate information whether or not the coating has popped-up during unloading;
- Cross-sectional electron microscopy of nanoindentations is a powerful method for the investigation of the failure mechanisms of coated systems subjected to nanoindentations;
- The WC/C system responds to release of the elastic strain energy by crack propagation in the carbon layers rather than by interfacial fracture;
- The hardness of the WC/C is found to be ~14 GPa and the effective Young's modulus is ~220 GPa;
- The good performance of the WC/C multilayers is attributed to low friction and stress levels offered by their ductility properties. The carbon lamellae reduce the friction and most likely the surface temperature. Thus, the wear rate is also reduced;
- The fact that the WC/C coating is eventually consumed, even under mild conditions and low wear rates, makes it an unsuitable choice in tribological applications of long-term use. Nevertheless, it is beneficial under emergency running situations, giving a low friction coefficient and a relative extensive lifetime;

- The main mechanism of coating failure under rolling contact fatigue conditions is exfoliation of the surface due to decohesion of the multilayers, rather than spalling fatigue by debonding along the interface;
- The investigation of the various coated systems revealed important clues regarding the impact of the different design of coating/substrate composites on their mechanical behaviour. From the microstructural characterisation and the mechanical performances studied in this chapter, it can be concluded that the system T1 (cf. figure 3.6c) appears to be the most promising for industrial applications.

References

1. G.M. Pharr, Mater. Sci. Engineering A **253**, 151 (1998).
2. T.F. Page, S.V. Hainsworth, Surf. Coatings Technol. **61**, 201 (1993).
3. T. Wright, T.F. Page, Surf. Coatings Technol. **54-55**, 557 (1992).
4. N.X. Randall, C.J. Schmutz, J.M. Soro, Surf. Coatings Technol. **108-109**, 489 (1998).
5. S.V. Hainsworth, M.R. McGurk, T.F. Page, Surf. Coatings Technol. **102**, 97 (1998).
6. M.R. McGurk, H.W. Chandler, P.C. Twigg, T.F. Page, Surf. Coatings Technol. **68-69**, 576 (1994).
7. E. Bergmann, J. Vogel, J. Vac. Sci. Technol. A **4**, 2867 (1986).
8. H. Dimigen, C.-P. Klages, Surf. Coatings Technol. **49**, 543 (1991).
9. K.L. Johnson, *Contact Mechanics*, Cambridge University press, (1985).
10. A.J. Whitehead, T.F. Page, Thin Solid Films **220**, 277 (1992).
11. S.V. Hainsworth, T.F. Page, Mat. Res. Soc. Symp. Proc. **436**, 171 (1997).
12. M.R. McGurk, T.F. Page, J. Mater. Res. **14**, 2283 (1999).
13. J. Franks, K. Enke, A. Richardt, Metals and Materials **11**, 695 (1990).
14. M. Ham, A. Lou, J. Vac. Sci. Technol. **A8**, 2143 (1990).
15. A. Raveh, L. Martinu, H.M. Hawthorne, M.R. Wertheimer, Surf. Coatings Technol. **58**, 45 (1993).
16. A. Matthews, A. Leyland, K. Holmberg, H. Ronkainen, Surf. Coatings Technol. **100-101**, 1 (1998).
17. K. Holmberg, A. Matthews, *Coatings Tribology*, Tribology Series 28, D. Dowson (ed.), Elsevier, Amsterdam, (1994).
18. O. Wänstrand, M. Larsson, P. Hedenqvist, Surf. Coatings Technol. **111**, 247 (1999).